BRIEF PAPER

Image Expansion Approach for Target Buried in Dielectric Medium with Extended RPM to Multi-Static UWB Radar

Yoshihiro NIWA[†a)], ***Student Member***, **Shouhei KIDERA**[†], ***and*** **Tetsuo KIRIMOTO**[†], ***Members***

SUMMARY Ultra wideband radar is one of the most promising techniques for non-invasive imaging in a dielectric medium, which is suitable for both medical screening and non-destructive testing applications. A novel imaging method for such an application is proposed in this brief paper, which has been extended from the advanced range points migration method to a multi-static observation model with circular arrays. One notable feature of this method is that it is applicable to either arbitrary dielectric or internal object shapes, and it can also expand the reconstructible image region compared with that obtained using the mono-static model by employing received signals after penetrating various propagation paths in dielectric medium. Numerical results for the investigation of an elliptical object, surrounded by a random dielectric surface, show the remarkable advantages of the proposed method with respect to image expansion.

key words: *UWB radars, range points migration (RPM), multi-static observation, internal imaging for dielectric medium*

1. Introduction

Ultra wideband (UWB) pulse radar has high range resolution and this UWB pulse has high dielectric permeability, and it is thus promising for use in non-invasive imaging applications, such as non-destructive testing of pipes buried in soil or in a concrete wall, or tumor detection in early-stage breast cancer. Various imaging methods are available for near-field UWB radar systems, including synthetic aperture radar (SAR) [1], beam forming based reconstruction [2], time reversal focusing [3], or the numerical solution of the domain integral equation with multi-dimensional optimization [4]. However, none of these methods can accomplish a good performance balance between the amount of computation required, and the desired accuracy or spatial resolution.

As a solution to this difficulty, we have already proposed a fast and accurate imaging method [6] for targets buried in a dielectric medium, by advancing the range points migration (RPM) method [5]. This performs accurate surface extraction for targets in free space by using the group mapping from the range points (a set of antenna locations and observed ranges) to target surface points [5]. The method [6] first uses the boundary points of the dielectric medium and their normal vectors, which can be accurately determined by RPM, and then the internal target points are reproduced by assessing the accumulation degree of potential target points by using a geometrical optics approximation. One notable feature of this method is that it can enhance the imaging speed remarkably without use of a signal integration approach, and improves the accuracy of target boundary extraction to the order of 1/100 of a wavelength.

However, the previous method [6] assumes a mono-static configuration in the observation, and often barely reconstructs the whole of the target boundary, particularly for a dielectric medium with a random surface (including concave region). This is because the instantaneous aperture size (defined as the actual area of the antenna being distributed at same instant) in the mono-static model is extremely small, whereas the equivalent aperture size is sufficiently large. This then poses difficulty in distinguishing the exact shape of an internal target, which could be critical in applications such as discrimination of a deformed pipe in a non-destructive testing application. To enhance the imaging area of an internal target, this brief paper introduces a novel method based on multi-static observation, where the principle of the method in [6] is appropriately extended to a single-transmitting and multiple-receiving model. This extension enables us to enhance the instantaneous aperture size, which helps in obtaining reflection echoes from a wider part of the target boundary, according to the combination of transmitting and receiving antennas. The results from numerical simulations show that the proposed method accurately expands the imaging region of the internal target, compared with that obtained using the mono-static based method, even for a dielectric medium with a concave surface.

2. System Model

Figure 1 shows the system model of a multi-static observation. We assume that the target and the dielectric medium with uniform permittivity have arbitrary shapes with clear boundaries, and the relative permittivity is given as ϵ_r. The propagation speed c of a radio wave in air is a known constant. The TE (Transverse Electric) mode wave is assumed. A number of omni-directional antennas are arranged on the circumference of circle, the inner region of which completely surrounds a dielectric medium. The current waveform induced at the transmitting antenna is a mono-cycle pulse with the central wavelength denoted as λ. The real space in which the target and the antennas are located is defined by the parameter $\boldsymbol{r} = (x, z)$. $s(\boldsymbol{r}_\mathrm{T}, \boldsymbol{r}_\mathrm{R}, R)$ is defined as the output of the Wiener filter, where the transmitting and receiving antennas are located at $\boldsymbol{r}_\mathrm{T} = (X_\mathrm{T}, Z_\mathrm{T})$ and

Manuscript received July 3, 2012.
Manuscript revised September 11, 2012.

[†]The authors are with the Graduate School of Informatics and Engineering, The University of Electro-Communications, Chofu-shi, 182-8585 Japan.
a) E-mail: niwa@secure.ee.uec.ac.jp

DOI: 10.1587/transele.E96.C.119

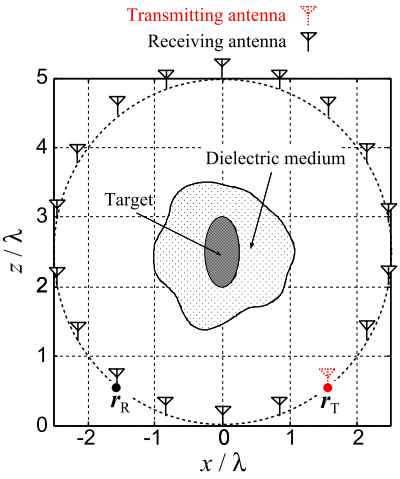

Fig. 1 System model in multi-static observation.

$\boldsymbol{r}_{\mathrm{R}} = (X_{\mathrm{R}}, Z_{\mathrm{R}})$, respectively, and $R = ct/2$ is expressed using time t. In the multi-static model, one antenna transmits a pulse and the other antennas receive a reflection echo at the same instant, and the location of the transmitting antenna is subsequently switched to a different location of array arrangement. The range points are defined as $\boldsymbol{q} = (\boldsymbol{r}_{\mathrm{T}}, \boldsymbol{r}_{\mathrm{R}}, R)$ and are extracted from the local maxima of $s(\boldsymbol{r}_{\mathrm{T}}, \boldsymbol{r}_{\mathrm{R}}, R)$, the details of this process are described in [5].

3. Conventional Method

This section briefly describes the conventional method [6] for comparison. This method assumes mono-static observation as shown in Fig. 2, and first extracts the range points as $\boldsymbol{q}_{\mathrm{S},j} = (\boldsymbol{r}_{\mathrm{T},j}, \boldsymbol{r}_{\mathrm{R},j}, R_{\mathrm{S},j})$, where $R_{\mathrm{S},j}$ having a minimum R for each antenna location and $\boldsymbol{r}_{\mathrm{T},j} = \boldsymbol{r}_{\mathrm{R},j}$ holds, because the noisy components can be eliminated by the range points extraction in [5], when the certain level of S/N is obtained. The dielectric boundary points $\boldsymbol{r}_{\mathrm{S},j} = (x_{\mathrm{S},j}, z_{\mathrm{S},j})$ are then reproduced by RPM [5], and are regarded as candidates for the incident points on the dielectric medium boundary. Here, all of the range points except for $\boldsymbol{q}_{\mathrm{S},j}$ are defined as $\boldsymbol{q}_i = (\boldsymbol{r}_{\mathrm{T},i}, \boldsymbol{r}_{\mathrm{R},i}, R_i)$. As a notable feature of RPM, each normal vector $\boldsymbol{e}_{\mathrm{N},j}$ on the RPM boundary points $\boldsymbol{r}_{\mathrm{S},j}$ can be calculated without a differential operation [6], and then, the potential target points $\boldsymbol{r}_{\mathrm{M}}(\boldsymbol{r}_{\mathrm{S},j}, \boldsymbol{q}_i)$ corresponding to $\boldsymbol{q}_i$ can be calculated as follows.

$$\boldsymbol{r}_{\mathrm{M}}(\boldsymbol{r}_{\mathrm{S},j}, \boldsymbol{q}_i) = \boldsymbol{r}_{\mathrm{S},j} + \frac{R_i - R_1(\boldsymbol{r}_{\mathrm{S},j}, \boldsymbol{q}_i)}{\sqrt{\epsilon_r}} \boldsymbol{e}_{\mathrm{T},j}(\boldsymbol{q}_i), \tag{1}$$

where $R_1(\boldsymbol{r}_{\mathrm{S},j}, \boldsymbol{q}_i) = \|\boldsymbol{r}_{\mathrm{T},i} - \boldsymbol{r}_{\mathrm{S},j}\|$, $\boldsymbol{e}_{\mathrm{T},j}(\boldsymbol{q}_i)$ denotes the transmissive direction, which is easily calculated using $\boldsymbol{e}_{\mathrm{N},j}$ by Snell's law. Figure 3 shows the spatial relationship among the antenna, dielectric boundary and target boundary points assumed i n mono-static observation. The method assumes that the target point exists in the set of $\boldsymbol{r}_{\mathrm{M}}(\boldsymbol{r}_{\mathrm{S},j}, \boldsymbol{q}_i)$ and the optimal point among them is determined as:

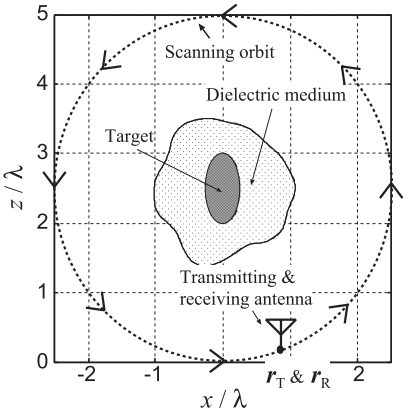

Fig. 2 System model in mono-static observation.

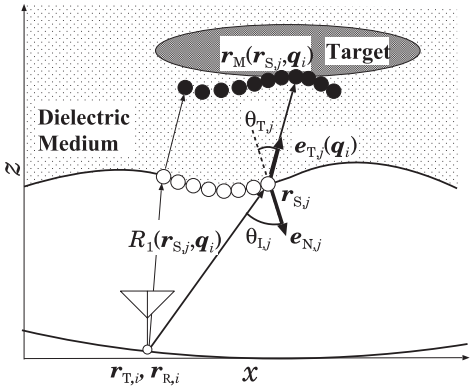

Fig. 3 Spatial relationship among antennas, dielectric boundary and target points in mono-static model.

$$\hat{\boldsymbol{r}}_{\mathrm{M}}(\boldsymbol{q}_i) = \underset{\boldsymbol{r}_{\mathrm{M}}(\boldsymbol{r}_{\mathrm{S},j}, \boldsymbol{q}_i)}{\arg\max} \sum_{l=1}^{N_M} s(\boldsymbol{q}_l) \exp\left(-\frac{\|\boldsymbol{r}_{\mathrm{T},i} - \boldsymbol{r}_{\mathrm{T},l}\|^2}{2\sigma_D^2} - \frac{(R_i - R_l)^2}{2\sigma_R^2}\right) \times \exp\left(-\frac{\min_k \|\boldsymbol{r}_{\mathrm{M}}(\boldsymbol{r}_{\mathrm{S},j}, \boldsymbol{q}_i) - \boldsymbol{r}_{\mathrm{M}}(\boldsymbol{r}_{\mathrm{S},k}, \boldsymbol{q}_l)\|^2}{2\sigma_r^2}\right), \tag{2}$$

where σ_D, σ_R and σ_r are empirically determined constants, and N_M denotes the total number of $\boldsymbol{q}_i$. While this method provides an accurate internal target image with a lower computational cost, it has been confirmed that the reconstructible region is often insufficient to identify the exact target shape, because part of the inner target falls into shadow in some cases as demonstrated in Sect. 5. This is because the instantaneous aperture size of this observation model is extremely small, namely, just one size of a single antenna, whereas a satisfactory equivalent aperture size is obtained by scanning a mono-static radar.

4. Proposed Method

To overcome the above difficulty, this section introduces an image expansion scheme using the multi-static observation model. This model maintains a large instantaneous aperture size, indicated Fig. 1. Then, by considering different combinations of transmitting and receiving antennas, the re-

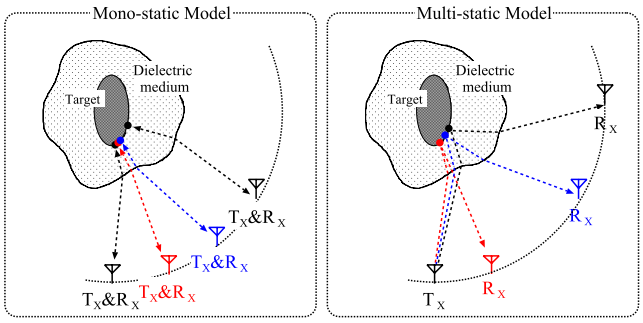

Fig. 4 Image expansion scheme by extending to multi-static observation model.

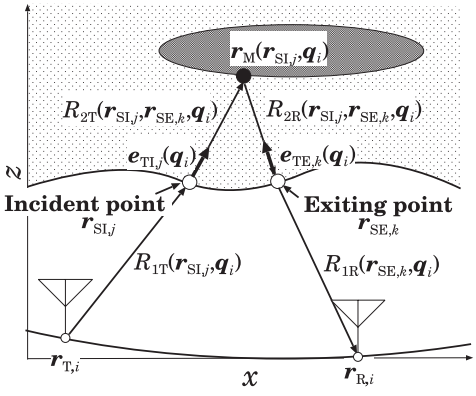

Fig. 5 Possible propagation path in multi-static observation.

ceived signals after propagating along various internal paths can be used for imaging. Figure 4 shows the image expansion scheme in an extension to the multi-static model. Since the imaging principle itself is similar to the conventional method, we focus on the formulation specific to the multi-static model, as follows. In the multi-static observation, it is predicted that the incident points defined as $\boldsymbol{r}_{\mathrm{SI},j}$ and the exit points defined as $\boldsymbol{r}_{\mathrm{SE},k}$ on the dielectric boundary have different locations, and thus a pairing process for them is needed in this model. Figure 5 shows the possible propagation path under multi-static observation. Using the normal vector on each dielectric point, the intersection point between the incident and exit paths can be calculated as $\boldsymbol{r}_{\mathrm{M}}(\boldsymbol{r}_{\mathrm{SI},j}, \boldsymbol{q}_i)$ shown in Fig. 5. Then, the propagation ranges in the dielectric medium given as $R_{2\mathrm{T}} = \|\boldsymbol{r}_{\mathrm{SI},j} - \boldsymbol{r}_{\mathrm{M},j}\|$ and $R_{2\mathrm{R}} = \|\boldsymbol{r}_{\mathrm{SE},k} - \boldsymbol{r}_{\mathrm{M},j}\|$ are determined as:

$$\begin{bmatrix} R_{2\mathrm{T}}(\boldsymbol{r}_{\mathrm{SI},j}, \boldsymbol{r}_{\mathrm{SE},k}, \boldsymbol{q}_i) \\ R_{2\mathrm{R}}(\boldsymbol{r}_{\mathrm{SI},j}, \boldsymbol{r}_{\mathrm{SE},k}, \boldsymbol{q}_i) \end{bmatrix} = \sqrt{\varepsilon_r}\left[\boldsymbol{e}^T_{\mathrm{TI},j}(\boldsymbol{q}_i), -\boldsymbol{e}^T_{\mathrm{TE},k}(\boldsymbol{q}_i)\right]^{-1}\left(\boldsymbol{r}^T_{\mathrm{SE},k} - \boldsymbol{r}^T_{\mathrm{SI},j}\right), \quad (3)$$

where $\boldsymbol{e}_{\mathrm{TI},j}(\boldsymbol{q}_i)$ and $\boldsymbol{e}_{\mathrm{TE},k}(\boldsymbol{q}_i)$ denote the penetration directions from $\boldsymbol{r}_{\mathrm{SI},j}$ and $\boldsymbol{r}_{\mathrm{SE},k}$, respectively, which are determined in a similar way to the method [6] by Snell's law. Using $R_{2\mathrm{T}}$ and $R_{2\mathrm{R}}$, the desired exit point as $\hat{\boldsymbol{r}}_{\mathrm{SE}}(\boldsymbol{r}_{\mathrm{SI},j}, \boldsymbol{q}_i)$ is determined as:

$$\hat{\boldsymbol{r}}_{\mathrm{SE}}(\boldsymbol{r}_{\mathrm{SI},j}, \boldsymbol{q}_i) = \arg\min_{\boldsymbol{r}_{\mathrm{SE},k}} \left|R_i - \tilde{R}(\boldsymbol{r}_{\mathrm{SI},j}, \boldsymbol{r}_{\mathrm{SE},k}, \boldsymbol{q}_i)\right|, \quad (4)$$

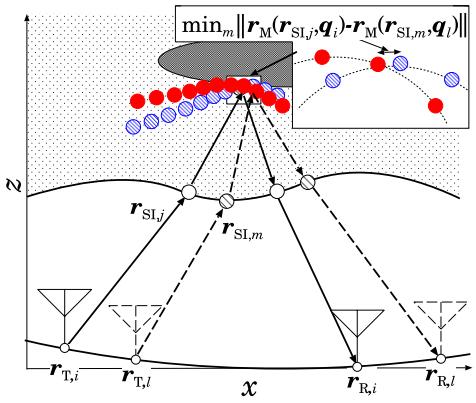

Fig. 6 Spatial relationship between the two groups of the candidate points $\boldsymbol{r}_{\mathrm{M}}(\boldsymbol{r}_{\mathrm{SI},j}, \boldsymbol{q}_i)$ and $\boldsymbol{r}_{\mathrm{M}}(\boldsymbol{r}_{\mathrm{SI},m}, \boldsymbol{q}_l)$.

where $\tilde{R}(\boldsymbol{r}_{\mathrm{SI},j}, \boldsymbol{r}_{\mathrm{SE},k}, \boldsymbol{q}_i) = R_{1\mathrm{T}}(\boldsymbol{r}_{\mathrm{SI},j}, \boldsymbol{q}_i) + R_{1\mathrm{R}}(\boldsymbol{r}_{\mathrm{SE},k}, \boldsymbol{q}_i) + R_{2\mathrm{T}}(\boldsymbol{r}_{\mathrm{SI},j}, \boldsymbol{r}_{\mathrm{SE},k}, \boldsymbol{q}_i) + R_{2\mathrm{R}}(\boldsymbol{r}_{\mathrm{SI},j}, \boldsymbol{r}_{\mathrm{SE},k}, \boldsymbol{q}_i)$, $R_{1\mathrm{T}}(\boldsymbol{r}_{\mathrm{SI},j}, \boldsymbol{q}_i) = \|\boldsymbol{r}_{\mathrm{T},i} - \boldsymbol{r}_{\mathrm{SI},j}\|$ and $R_{1\mathrm{R}}(\boldsymbol{r}_{\mathrm{SE},k}, \boldsymbol{q}_i) = \|\boldsymbol{r}_{\mathrm{R},i} - \boldsymbol{r}_{\mathrm{SE},k}\|$. For each $\boldsymbol{q}_i$, the potential target points $\boldsymbol{r}_{\mathrm{M}}(\boldsymbol{r}_{\mathrm{SI},j}, \boldsymbol{q}_i)$ are calculated:

$$\boldsymbol{r}_{\mathrm{M}}(\boldsymbol{r}_{\mathrm{SI},j}, \boldsymbol{q}_i) = \boldsymbol{r}_{\mathrm{SI},j} + \frac{R_{2\mathrm{T}}(\boldsymbol{r}_{\mathrm{SI},j}, \hat{\boldsymbol{r}}_{\mathrm{SE}}(\boldsymbol{r}_{\mathrm{SI},j}, \boldsymbol{q}_i), \boldsymbol{q}_i)}{\sqrt{\epsilon_r}} \boldsymbol{e}_{\mathrm{TI},j}(\boldsymbol{q}_i). \quad (5)$$

Based on a similar approach to the method of [6], the optimum candidate for the internal target point $\hat{\boldsymbol{r}}_{\mathrm{M}}(\boldsymbol{q}_i)$ is calculated as

$$\hat{\boldsymbol{r}}_{\mathrm{M}}(\boldsymbol{q}_i) = \arg\max_{\boldsymbol{r}_{\mathrm{M}}(\boldsymbol{r}_{\mathrm{SI},j}, \boldsymbol{q}_i)} \sum_{l=1}^{N_M} s(\boldsymbol{q}_l) \exp\left(-\frac{D^2_{i,l}}{2\sigma^2_D} - \frac{(R_i - R_l)^2}{2\sigma^2_R}\right) \times \exp\left(-\frac{\min_m \|\boldsymbol{r}_{\mathrm{M}}(\boldsymbol{r}_{\mathrm{SI},j}, \boldsymbol{q}_i) - \boldsymbol{r}_{\mathrm{M}}(\boldsymbol{r}_{\mathrm{SI},m}, \boldsymbol{q}_l)\|^2}{2\sigma^2_r}\right), \quad (6)$$

where $D_{i,l} = \min\left(\|\boldsymbol{r}_{\mathrm{T},i} - \boldsymbol{r}_{\mathrm{T},l}\| + \|\boldsymbol{r}_{\mathrm{R},i} - \boldsymbol{r}_{\mathrm{R},l}\|, \right.$ $\left.\|\boldsymbol{r}_{\mathrm{T},i} - \boldsymbol{r}_{\mathrm{R},l}\| + \|\boldsymbol{r}_{\mathrm{R},i} - \boldsymbol{r}_{\mathrm{T},l}\|\right)$ holds. Figure 6 depicts the spatial relationship between the two groups of candidate points, $\boldsymbol{r}_{\mathrm{M}}(\boldsymbol{r}_{\mathrm{SI},j}, \boldsymbol{q}_i)$ and $\boldsymbol{r}_{\mathrm{M}}(\boldsymbol{r}_{\mathrm{SI},m}, \boldsymbol{q}_l)$. Equation (6) assesses the accumulation degree of the intersection points of the candidate curves, which is regarded as the advanced principle of the original RPM.

5. Performance Evaluation of Numerical Simulation

This section presents performance examples for each method in numerical simulation. Here, the FDTD (finite difference time domain) method is used for received data generation. The relative permittivity and conductivity of the dielectric medium are set to 5 and 0.005 S/m. The fractional bandwidth of the transmitted mono-cycle pulse is about 150%, which is in accord with the definition of UWB pulse [7]. Figures 7 and 8 show the estimated dielectric and internal target boundaries obtained by the conventional (mono-static) and proposed (multi-static) methods, respectively, where the same antenna arrangement or the scanning orbit are used in each model as shown in Figs. 1 and 2, respectively. Gaussian white noise has been added to the received signals. The signal to noise ratio (S/N) is defined as

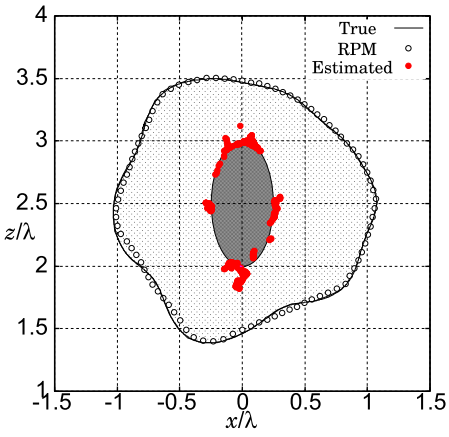

Fig. 7 Dielectric and target boundary images obtained by the conventional method at S/N = 30 dB.

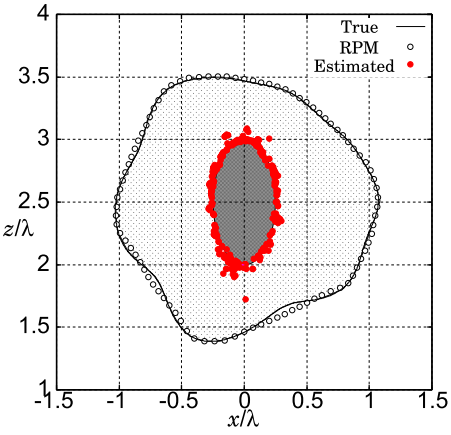

Fig. 8 Dielectric and target boundary images obtained by the proposed method at S/N = 30 dB.

the ratio of the peak instantaneous signal power to the average noise power, after application of a matched filter. In this case, S/N = 30 dB is assumed. For an equitable assessment in the comparison of the two methods, the number of observation points is set at 720 for the conventional model, and the number of array antennas is 36 for the proposed model, i.e. the number of combination from 36 chose 2, ${}_{36}C_2 = \dfrac{36!}{34! \times 2!} = 630$ independent data are usable. Here, $\sigma_D = 0.5\lambda$, $\sigma_R = 1.0\lambda$, $\sigma_r = 0.05\lambda$ are set parameters in both methods. The results here prove that while the conventional method cannot obtain the whole target boundary. This is because any antenna, even densely distributed around the circular circumference, cannot receive reflection echoes from the particular region of the target boundary. The reason is that the propagation path in the dielectric medium is skewed at the dielectric boundary, and at certain times all skewed propagation paths are unable to reach one particular area of the inner target boundary. This effect arises for not only concave boundaries but also convex boundaries of dielectric medium. On the contrary, our proposed method dramatically enhances the reconstructible region without significant degradation in accuracy by recording the received signal after propagating along various internal paths.

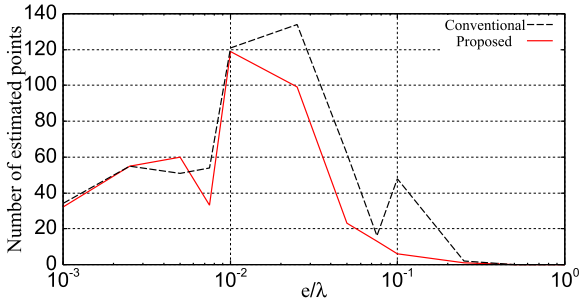

Fig. 9 Comparison of the number of estimated target points obtained by each method at S/N = 30 dB.

Table 1 Comparison for imaging performance in each method.

	RMSE ($\times 10^{-2}\lambda$)	Reconstructible ratio(P_a) [%]
Conventional(Mono-static)	4.78	59.1
Proposed(Multi-static)	2.84	99.5

For quantitative evaluation of the images obtained, an error value is introduced as

$$\mathrm{e} = \min_{\boldsymbol{r}_{\mathrm{true}}} \|\boldsymbol{r}_{\mathrm{est},i} - \boldsymbol{r}_{\mathrm{true}}\|, (i = 1, 2, \ldots, N_{\mathrm{est}}) \tag{7}$$

where $\boldsymbol{r}_{\mathrm{true}}$ and $\boldsymbol{r}_{\mathrm{est},i}$ represent the locations of the true and estimated target points, respectively. N_{est} denotes the total number of estimated points, so that the sampling interval at the inner target boundary should be sufficiently smaller than 0.1λ. Figure 9 shows the number of estimated points for each e calculated from the target points obtained by each method. These results show that almost all of the target points satisfy $\mathrm{e} \leq 0.1\lambda$ in both methods. Also, for assessment of the possible imaging region, the evaluation value $P_{\mathrm{a}} = (N'_{\mathrm{est}}/N_{\mathrm{true}}) \times 100\,[\%]$ is introduced, where N_{true} denotes the number of true target points and N'_{est} expresses the number of estimated target points that satisfy $\mathrm{e} \leq \mathrm{e}_a$. Table 1 summarizes the above evaluations of both the conventional and the proposed methods, where $\mathrm{e}_a = 0.04\lambda$ is set and RMSE denotes the root mean square of e. This table quantitatively demonstrates that the proposed method significantly expands the imaging range with accuracy at the order of 1/100 of the wavelength. This is because a greater instantaneous aperture size in the multi-static model makes it possible to obtain echoes from the larger part of the internal target.

6. Conclusion

This brief paper proposed a novel image expansion method for targets buried in a dielectric medium, using the internal RPM method extended to the multi-static observation model. One distinct feature of this method is that it can expand the internal object imaging region, considerably by enhancing the instantaneous aperture size, even in a random

surface in a dielectric medium that includes a concave region. The results of a numerical simulation of a noisy scenario demonstrated that the proposed method enhances the imaging domain by around 40%, compared to that obtained by the conventional method, with suppression of the RMSE of the target reconstruction to within 0.03λ.

Acknowledgment

This work is supported by the Research Grant (Basic Research) promoted by TEPCO Memorial Foundation and the Research Research Grants offered by the Kurata Memorial Hitachi Science and Technology Foundation.

References

[1] R.M. Narayanan, X. Xu, and J.A. Henning, "Radar penetration imaging using ultra-wideband (UWB) random noise waveforms," IEE Proc. Radar Sonar Navig, vol.151, no.3, pp.143–148, 2004.

[2] M.O. Halloran, E. Jones, and M. Glavin, "Quasi-multistatic MIST beamforming for the early detection of breast cancer," IEEE Trans. Biomed. Eng., vol.57, no.4, pp.830–840, April 2010.

[3] A. Cresp, I. Aliferis, M.J. Yedlin, Ch. Pichot, and J.-Y. Dauvignac, "Investigation of time-reversal processing for surface-penetrating radar detection in a multiple-target configuration," Proc. EuRAD, 2008, pp.1–4, Nov. 2008.

[4] S.D. Rajan and G.V. Frisk, "A comparison between the Born and Rytov approximations for the inverse backscattering problem," Geophysics, vol.54, no.7, pp.864–871, 1989.

[5] S. Kidera, T. Sakamoto, and T. Sato, "Accurate UWB radar three-dimentional imaging algorithm for a complex boundary without range point connections," IEEE Trans. Geosci. Remote Sens., vol.48, no.7, pp.1993–2004, 2010.

[6] K. Akune, S. Kidera, and T. Kirimoto, "Accurate and nonparametric imaging algorithm for targets buried in dielectric medium for UWB radars," IEICE Trans. Electron., vol.E95-C, no.8, pp.1389–1398, Aug. 2012.

[7] Federal Communications Commission (FCC), Office of Engineering and Technology (OET) Bulletin no.65, Supplement C, Aug. 1997.